Title

Development of New Deoxycytidine Kinase Inhibitors and Noninvasive in Vivo Evaluation Using Positron Emission Tomography

Journal

Journal of Medicinal Chemistry, 56(17)

ISSN

0022-2623

Authors

Murphy, Jennifer M
Armijo, Amanda L
Nomme, Julian
et al.

Publication Date

2013-09-12

DOI

10.1021/jm400457y

Peer reviewed

Journal of Medicinal Chemistry

Article

pubs.acs.org/jmc

Development of New Deoxycytidine Kinase Inhibitors and Noninvasive in Vivo Evaluation Using Positron Emission Tomography

Jennifer M. Murphy,[‡,†,§,○] Amanda L. Armijo,[‡,†,§] Julian Nomme,[‡,∥] Chi Hang Lee,[†,§] Quentin A. Smith,[⊥] Zheng Li,[†,§] Dean O. Campbell,[†,§,▲] Hsiang-I Liao,[†,§] David A. Nathanson,[†,§] Wayne R. Austin,[†,§] Jason T. Lee,[†,§,◆] Ryan Darvish,[†,§] Liu Wei,[†,§] Jue Wang,[†,§] Ying Su,[∥] Robert Damoiseaux,[#] Saman Sadeghi,[†,§] Michael E. Phelps,[†] Harvey R. Herschman,[†,△] Johannes Czernin,[†,§] Anastassia N. Alexandrova,[⊥] Michael E. Jung,[⊥] Arnon Lavie,*[,∥] and Caius G. Radu*[,†,§]

[†]Department of Molecular and Medical Pharmacology, [§]Ahmanson Translational Imaging Division, [⊥]Department of Chemistry and Biochemistry, [#]California NanoSystems Institute, [△]Department of Biological Chemistry, University of California, Los Angeles, 650 Charles E. Young Dr. S., Los Angeles, California 90095, United States

[∥]Department of Biochemistry and Molecular Genetics, University of Illinois at Chicago, 900 S. Ashland Avenue, M/C 669, Chicago, Illinois 60607, United States

Supporting Information

ABSTRACT: Combined inhibition of ribonucleotide reductase and deoxycytidine kinase (dCK) in multiple cancer cell lines depletes deoxycytidine triphosphate pools leading to DNA replication stress, cell cycle arrest, and apoptosis. Evidence implicating dCK in cancer cell proliferation and survival stimulated our interest in developing small molecule dCK inhibitors. Following a high throughput screen of a diverse chemical library, a structure−activity relationship study was carried out. Positron Emission Tomography (PET) using ^{18}F-L-1-(2′-deoxy-2′-**F**luoro**A**rabinofuranosyl) **C**ytosine (^{18}F-L-FAC), a dCK-specific substrate, was used to rapidly rank lead compounds based on their ability to inhibit dCK activity *in vivo*. Evaluation of a subset of the most potent compounds in cell culture (IC_{50} = ∼1−12 nM) using the ^{18}F-L-FAC PET pharmacodynamic assay identified compounds demonstrating superior in vivo efficacy.

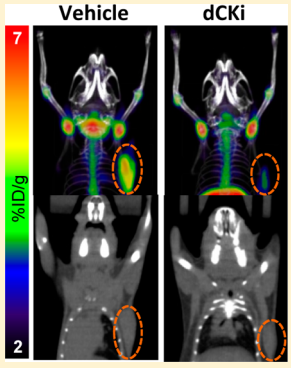

INTRODUCTION

Mammalian cells rely on two major pathways for the production and maintenance of deoxyribonucleotide triphosphates (dNTPs) for DNA replication and repair: the de novo pathway and the nucleoside salvage pathway.[1] The de novo pathway produces dNTPs from glucose and amino acids. The nucleoside salvage pathway produces dNTPs from preformed deoxyribonucleosides present in the extracellular environment.[1] The first enzymatic step in the cytosolic deoxyribonucleoside salvage pathway is catalyzed by deoxycytidine kinase (dCK) and by thymidine kinase 1 (TK1).[2] dCK catalyzes 5′-phosphorylation of deoxycytidine (dC), deoxyguanosine (dG), and deoxyadenosine (dA) to their monophosphate forms, exhibiting the highest affinity for dC.[3] The monophosphate deoxyribonucleotides are subsequently phosphorylated to their corresponding di- and triphosphate forms by other kinases.[4,5] We have shown that dCK and TK1 play important roles in hematopoiesis by regulating dNTP biosynthesis in lymphoid and erythroid progenitors.[6,7] In addition to its physiological role in nucleotide metabolism, dCK phosphorylates several clinically important antiviral and anticancer nucleoside analog prodrugs (e.g., gemcitabine, decitabine, fludarabine, cytarabine, clofarabine); phosphorylation by dCK is critically required for the activation of these prodrugs.[8] Recently, dCK was implicated in the regulation of the G2/M checkpoint in cancer cells in response to DNA damage.[9] The role of dCK in hematopoiesis and cancer has led to our interest in developing a small molecule inhibitor of this kinase. Such dCK inhibitors could represent new therapeutic agents for malignancies and immune disorders. To our knowledge, few dCK inhibitors have been reported,[10−12] and only one[13] has been demonstrated to inhibit dCK activity in vivo.

Positron emission tomography (PET) is a noninvasive in vivo imaging technique widely used for diagnosing, staging, restaging, and therapy monitoring of various diseases.[14,15] While PET using the radiotracer 2-^{18}F-fluoro-2-deoxy-D-glucose (^{18}F-FDG)[16,17] has become an important diagnostic and treatment monitoring tool in cancer,[18−21] another emerging application of PET concerns its use in drug discovery and development. Thus, by facilitating faster and more effective

Received: March 28, 2013
Published: August 15, 2013

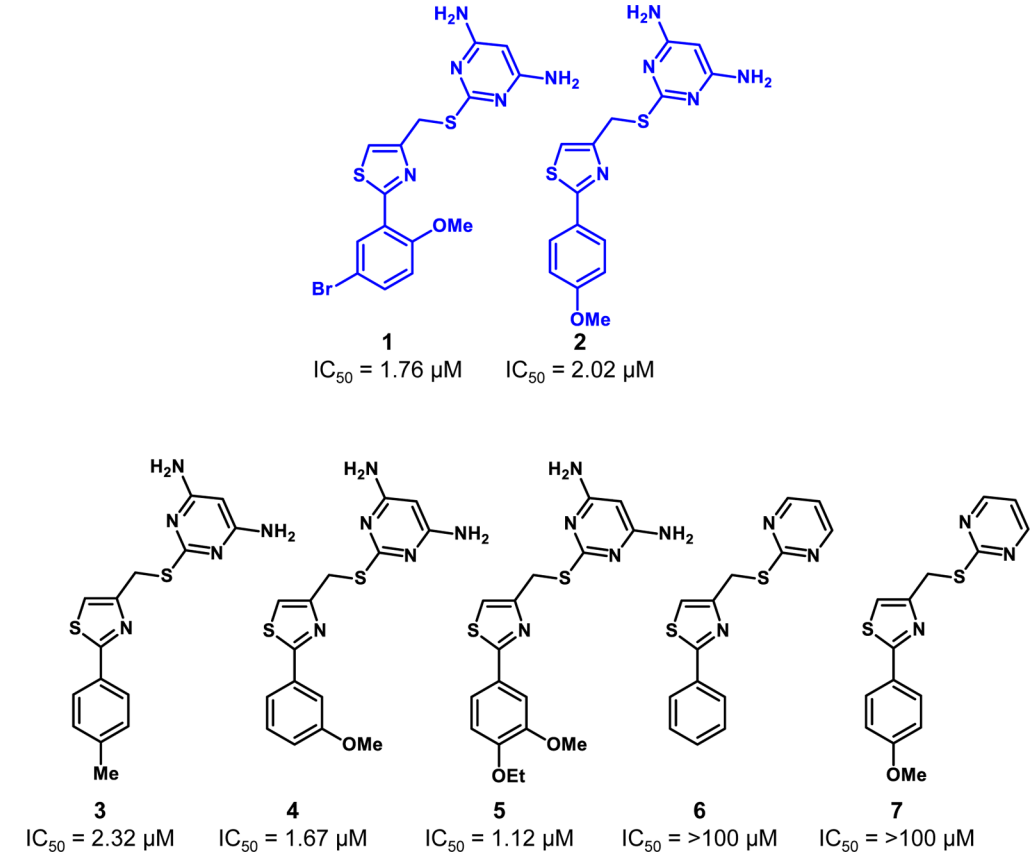

Figure 1. Structures and IC_{50} values determined using the ^{3}H-dC uptake assay in L1210 cells for the initial HTS hits (**1** and **2**) and for commercially available compounds containing similar structural scaffolds (**3**–**7**).

Table 1. In Vitro Biological Data in L1210 and CEM Cells for Compounds 8–14[a]

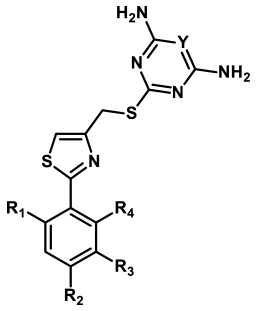

					IC_{50} (μM) L1210 cells		IC_{50} (μM) CEM cells	
compd	R_1	R_2	R_3	R_4	**a** Y = CH	**b** Y = N	**a** Y = CH	**b** Y = N
8	H	OCH_2CH_2F	OCH_3	H	0.808 (±0.406)	1.612 (±0.543)	0.421 (±0.075)	0.534 (±0.012)
9	H	OCH_3	OCH_2CH_2F	H	0.538 (±0.014)	0.528 (±0.015)	0.230 (±0.042)	0.506 (±0.138)
10	H	OCH_2CH_3	OCH_2CH_2F	H	0.513 (±0.100)	1.226 (±0.450)	0.251 (±0.020)	0.512 (±0.409)
11	H	CH_3	OCH_2CH_2F	H	2.381 (±0.042)	3.201 (±0.566)	1.960 (±1.001)	1.922 (±0.573)
12	H	OCH_3	$OCH_2CH_2CH_2F$	H	0.330 (±0.160)	0.603 (±0.140)	0.197 (±0.109)	0.297 (±0.020)
13	OCH_3	H	OCH_2CH_2F	H	1.445 (±0.060)	2.649 (±0.902)	1.041 (±0.084)	0.849 (±0.183)
14	H	OCH_2CH_2F	H	OCH_3	5.469 (±1.336)	ND[b]	2.367 (±0.238)	ND[b]

[a]Inhibitory activity measured by ^{3}H-deoxycytidine (^{3}H-dC) uptake in murine L1210 cells and in CCRF-CEM human cells. Values reported are the mean ± SD of at least n = 2 independent experiments. [b]ND = not determined (compound was not synthesized).

decision-making early in the drug discovery/development process, PET could accelerate the advancement of promising candidates and reduce failures.[22−24] For instance, PET can be used to demonstrate the need to modify lead candidates early in the drug discovery process by enabling noninvasive evaluations of drug pharmacodynamic (PD) and/or pharmacokinetic (PK) properties. In the specific context of our drug discovery and development program centered on dCK, PET could play a particularly important role given the availability of validated PET biomarkers to assess dCK activity in vivo. These

dx.doi.org/10.1021/jm400457y | J. Med. Chem. 2013, 56, 6696−6708

Table 2. In Vitro Biological Data in L1210 and CEM Cells for Compounds 15−18[a]

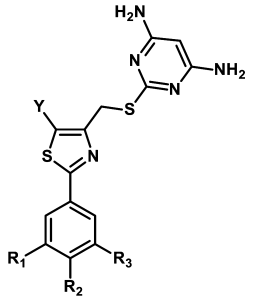

				IC_{50} (μM) L1210 cells			IC_{50} (μM) CEM cells		
compd	R_1	R_2	R_3	**a** Y = Me	**b** Y = Et	**c** Y = Pr	**a** Y = Me	**b** Y = Et	**c** Y = Pr
15	H	OCH_3	OCH_2CH_2F	0.035 (±0.015)	0.030 (±0.077)	0.003 (±0.000)	0.018 (±0.012)	0.007 (±0.002)	0.003 (±0.000)
16	F	H	F	0.595 (±0.163)	0.620 (±0.170)	0.385 (±0.262)	0.150 (±0.099)	0.162 (±0.019)	0.173 (±0.157)
17	H	F	H	0.395 (±0.134)	0.265 (±0.163)	0.170 (±0.099)	0.230 (±0.134)	0.083 (±0.043)	0.037 (±0.020)
18	H	H	F	0.255 (±0.021)	0.510 (±0.014)	0.175 (±0.007)	0.092 (±0.048)	0.011 (±0.038)	0.031 (±0.024)

[a]Inhibitory activity measured by ^{3}H-deoxycytidine (^{3}H-dC) uptake in murine L1210 and in CCRF-CEM human cells. Values reported are the mean ± SD of at least n = 2 independent experiments.

PET PD biomarkers of dCK activity include a series of ^{18}F-fluoro-arabinofuranosylcytosine analogs substrates of dCK developed by our group[25] which include ^{18}F-1-(2′-deoxy-2′-**F**luoro**A**rabinofuranosyl) **C**ytosine (^{18}F-FAC)[26] and ^{18}F-L-1-(2′-deoxy-2′-**F**luoro**A**rabinofuranosyl) **C**ytosine (^{18}F-L-FAC).[27] Herein we describe the development of potent dCK inhibitors and demonstrate their in vivo efficacy using ^{18}F-L-FAC PET as a noninvasive and clinically applicable PD biomarker.

RESULTS AND DISCUSSION

Identification of Lead Compound 15c. To identify new small molecule inhibitors of dCK, we performed a high throughput screen (HTS) of a set of selected chemical libraries totaling ∼90,000 small molecules. We screened the library for dCK inhibitory function using a Firefly luciferase-coupled assay with recombinant human dCK enzyme.[28] In this assay, inhibition of dCK prevents ATP depletion by dCK, thus resulting in higher luminescent signals in positive wells. The screen yielded two hit compounds, **1** and **2**, which were validated to inhibit the uptake of tritiated deoxycytidine (^{3}H-dC) with micromolar potency in the L1210 murine leukemia cell line (Figure 1).

Based on these results, five commercially available compounds containing similar structural scaffolds were tested; their IC_{50} values against L1210 cells were determined by measuring inhibition of ^{3}H-dC uptake (Figure 1). Strikingly, compounds **6** and **7** were inactive, suggesting that the bis-amino functionality on the pyrimidine ring is crucial for dCK inhibition. Based on these results, we initiated a structure−activity relationship (SAR) study to develop a lead structure, which could be further optimized to compounds with potent in vivo activity.

We initially studied two main structural classes of compounds, pyrimidines and 1,3,5-triazines (Table 1). Two cell lines were used to determine the IC_{50} values: the L1210 murine leukemia cells and the CCRF-CEM human acute T-lymphoblastic leukemia cells. In nearly all cases, substitution of the pyrimidine ring with the 1,3,5-triazine motif reduced dCK inhibitory activity; in some instances an approximate 2-fold reduction in potency was observed. Consequently, the pyrimidine motif was utilized as the preferred scaffold to advance. At this stage of the SAR, the presence of a fluoroethoxy side-chain on the phenyl ring was considered for eventual ^{18}F-radiolabeling purposes. Substitutions around the phenyl ring with respect to the position of the fluoroethoxy side-chain were also examined. Moving the fluoroethoxy side-chain from the para position in **8a** to the meta position in **9a** increased the inhibitory activity approximately 2-fold. It was also apparent that alkoxy substituents in the para position were better than alkyl moieties, since compound **11a** had substantially lower activity than either the methoxy **9a** or ethoxy **10a** analogs. Compound **12a**, which contains a side-chain that was extended by one carbon to give a fluoropropoxy group at the meta position, gave slightly greater inhibitory activity, albeit not a significant increase from compounds **9a** and **10a**. Substitution at the ortho position of the phenyl ring, e.g. in compounds **13a** and **14a**, resulted in substantially lower dCK inhibitory activity, an approximate 10-fold decrease in potency was observed for compound **14a** when compared to **9a**. A general synthetic scheme for compounds in Table 1 can be found in the Supporting Information (Scheme S2).

While the presence of fluorine in the small molecule may eventually enable the synthesis of an ^{18}F-isotopolog of the dCK inhibitor, fluorine introduction also affects nearly all the physical and ADME (adsorption, distribution, metabolism, and excretion) properties of a compound.[29] The capacity of fluorine to enhance metabolic stability has become increasingly apparent in recent years.[30] Thus, a series of compounds were synthesized which contained fluorine attached directly on the aromatic ring of the inhibitors rather than linked by an ethoxy side-chain (compounds **16**−**18**, Table 2). For each compound in this series, a set of three derivatives (**a**−**c**) were synthesized; in each case the group on the 5-position of the thiazole was either a methyl, ethyl, or propyl substituent. For compounds **15a**−**c** the fluoroethoxy side-chain was retained at the meta position of the phenyl ring, as was a methoxy group at the para position due to the favorable inhibitory results from the initial SAR in Table 1.

Increasing nonpolar functionality at the 5-position of the thiazole resulted in increasing inhibitory activity (Table 2). The IC_{50} values in CCRF-CEM cells illustrate the same trend in potency as observed in L1210 cells with one exception; set **16** shows little difference between the methyl, ethyl, or propyl

dx.doi.org/10.1021/jm400457y | J. Med. Chem. 2013, 56, 6696−6708

Scheme 1. Synthesis of Compounds 15a–c[a]

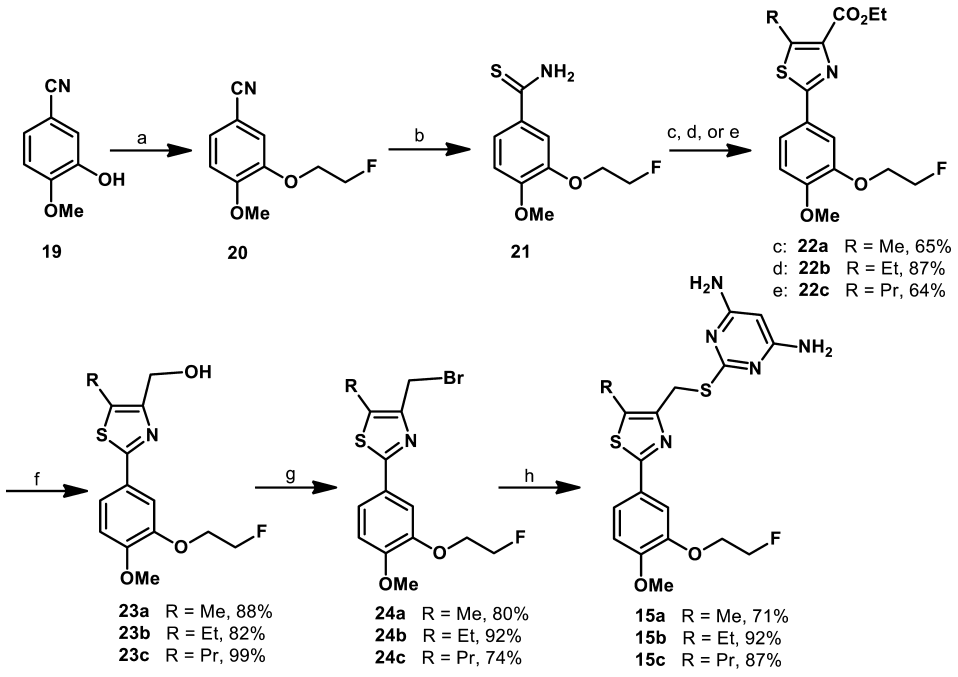

[a]Reagents and conditions: (a) 1-bromo-2-fluoroethane, Cs_2CO_3, DMF, 99%; (b) $(NH_4)_2S$ (20% in H_2O), pyridine, Et_3N, quantitative; (c) ethyl 3-bromo-2-oxobutanoate, EtOH; (d) ethyl 3-bromo-2-oxopentanoate, EtOH; (e) ethyl 3-bromo-2-oxohexanoate, EtOH; (f) DIBAL-H, CH_2Cl_2; (g) 1,1,1,3,3,3-hexabromoacetone, PPh_3, CH_3CN; (h) 4,6-diamino-2-mercaptopyrimidine, NaOH, EtOH.

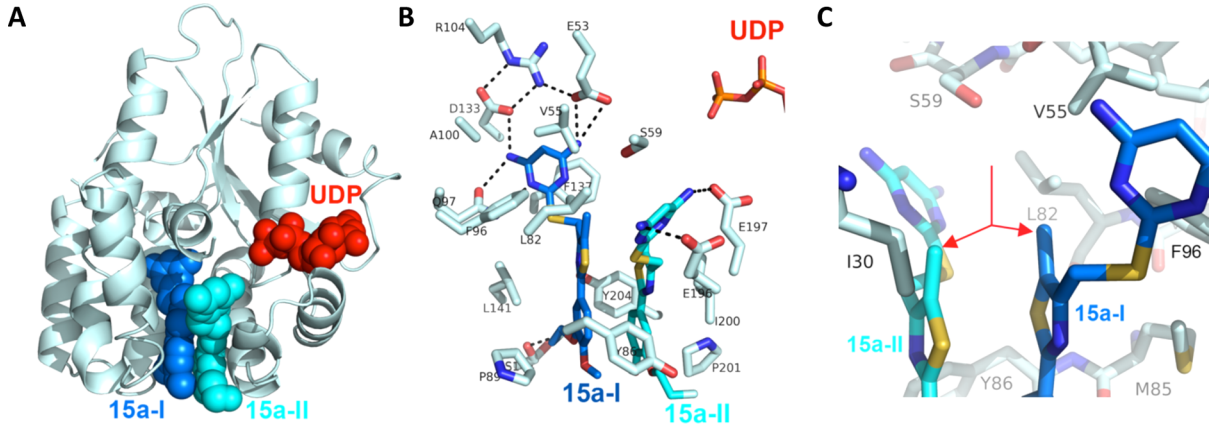

Figure 2. Binding of **15a** to human dCK. (A) Ribbon diagram of a dCK monomer (light blue) with the two observed molecules of **15a** bound (blue and cyan spheres, respectively) at the active site. The nucleotide UDP (red) was also present in the complex. (B) The interactions between **15a** and dCK. Polar interactions are indicated as broken black lines. The two phosphate groups of UDP (top right) demonstrate the relative orientation of **15a-I** (blue) and **15a-II** (cyan) to the nucleotide. (C) The methyl group of the **15a-I** and **15a-II** thiazole ring (red arrows) stack against each other, occupying a hydrophobic pocket.

substituents. However, for all compounds tested against L1210 cells, the propyl substituent yielded better inhibitory activity than the corresponding methyl derivatives. The best example in L1210 cells was the 12-fold increase in activity when comparing compound **15c** to compound **15a**. In addition, comparisons between the propyl substituents against their respective methyl derivatives in CCRF-CEM cells also showed an increasing inhibitory trend in activity: 6-fold (compare **17c** to **17a**) or 3-fold (compare **18c** to **18a**). The most drastic effect from modifications at the 5-position of the thiazole ring was the change exhibited from **9a** in Table 1 to **15c** in Table 2, where the substitution of a hydrogen for a propyl moiety resulted in a 180-fold increase in potency in L1210 cells. In addition, removal of the fluoroethoxy side-chain (e.g., compound series **16**–**18**) resulted in a significant decrease in potency in both cell lines. Compound **15c**, the most potent compound in this series, contains both the fluoroethoxy side-chain at the meta position on the phenyl ring and also a propyl group at the 5-position of the thiazole ring.

Synthesis. Compounds **15a–c** were synthesized in six steps (Scheme 1). The commercially available 3-hydroxy-4-methoxybenzonitrile **19** was functionalized via alkylation with 1-bromo-2-fluoroethane in DMF with cesium carbonate as the base to obtain the nitrile **20** in 99% yield. Subjection of **20** to an aqueous ammonium sulfide solution under basic conditions afforded the thioamide **21** in excellent yield.[31] Cyclization to

dx.doi.org/10.1021/jm400457y | J. Med. Chem. 2013, 56, 6696–6708

A

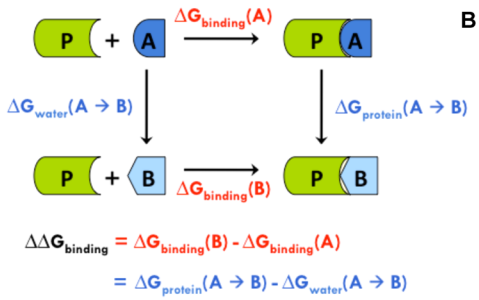

B

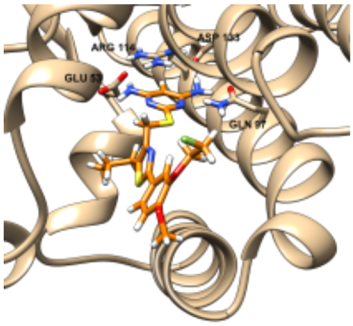

C

	$\Delta G_{protein}$	ΔG_{water}	$\Delta\Delta G_{binding}$
15b to **15c**	1.964 ± 0.050	2.802 ± 0.046	-0.838 ± 0.068
15c to **15b**	-1.251 ± 0.029	-2.832 ± 0.046	1.581 ± 0.054
Average			1.210 in favor of **15c**

Figure 3. (A) The complete thermodynamic cycle relating the binding energies to the perturbation of molecule A into molecule B. Δ*G*protein(A → B) denotes the change in free energy upon perturbation of A into B in the solvated inhibitor−protein complex, while Δ*G*water(A → B) denotes the free energy change when the perturbation takes place in water alone. The difference in free energies of binding, ΔΔ*G*binding, is equal to the change in free energy when molecule A binds with the protein [Δ*G*binding(A)] subtracted from the change in free energy when molecule B binds [Δ*G*binding(B)]. Because the sum of all components in a complete thermodynamic cycle must equal zero, ΔΔ*G*binding is therefore also equivalent to Δ*G*protein(A → B) − Δ*G*water(A → B). (B) Computational model of compound **15c** (orange) in complex with dCK. Binding pocket residues Glu 53, Gln 97, Arg 114, and Asp 133 are shown explicitly, while the remainder of the protein is illustrated as a ribbon structure. (C) Free energy changes (kcal/mol) associated with the perturbation of the alkyl chain at the 5-position of the thiazole. Δ*G*protein is the change in free energy for the solvated inhibitor−protein complex. Δ*G*water is the free energy change for the inhibitor in water alone. The change in free energy upon binding is denoted as ΔΔ*G*binding.

form the thiazole core of **15a−c** was achieved via condensation of thioamide **21** with the respective ethyl 3-bromo-2-oxoalkanoate[32] in refluxing ethanol.[33] Reduction of the resulting compounds with diisobutylaluminum hydride afforded the respective alcohols **23a−c** in 88−99% yield. The alcohols **23a−c** were converted to the respective bromides **24a−c** under mild conditions[34] in 74−80% yield. Finally, nucleophilic displacement of the bromide with 4,6-diamino-2-mercaptopyrimidine[35] generated the desired products **15a−c** in 71−87% yield.

X-ray Crystal Structure of Compound 15a Bound to Human dCK. X-ray crystallographic studies of compound **15a** were initiated to obtain information about its binding to dCK. Detailed analysis of the dCK-inhibitor interactions for this series of compounds was performed (Nomme, unpublished results). In short, the crystal structure of the dCK:**15a** complex was solved at 1.9 Å resolution (Figure 2). Human dCK, a dimer of two identical subunits with a molecular weight of ∼30 kDa per monomer, can bind either ATP or UTP as the phosphoryl donor for catalysis; in addition, dCK can adopt an open or closed conformation.[36,37,3] In complex with **15a**, the enzyme adopts the open conformation. We observed two **15a** molecules in each protomer of the dimeric enzyme (shown in blue (**15a-I**) and cyan (**15a-II**), Figure 2A). Note that binding of **15a** to dCK does not preclude nucleotide binding (UDP is shown in red, Figure 2A). The parallel orientation between **15a-I** and **15a-II** allows for optimal $\pi-\pi$ stacking interactions between the phenyl and thiazole rings of each molecule.

While two molecules of **15a** bind in the active site, it appears that **15a-I** forms more key interactions and shorter hydrogen bond distances than **15a-II** (Figure 2B). The extensive hydrogen-bond network that exists between the pyrimidine moiety of **15a-I** and residues E53, Q97, and D133 in the dCK nucleoside binding site are illustrated in Figure 2B. Figure 2C illustrates the hydrophobic pocket that exists, via V55, L82, and F96, around the methyl group of compound **15a**. This figure demonstrates that the pocket will accept larger substituents, explaining the increased trend in potency obtained for compounds **15b** and **15c**.

Monte Carlo-Based Computational Modeling. A Monte Carlo[38] (MC)-based computational modeling approach using the free energy perturbation (FEP) method[39,40] was used to further investigate the inhibitory effects of alkyl chain lengthening at the 5-position of the thiazole. FEP allows calculation of the difference in binding energy of two molecules. The perturbation of molecule **A** into molecule **B** in a complex with a protein [$\Delta G_{protein}$(A → B)] and in solution alone [ΔG_{water}(A → B)] is part of a complete thermodynamic cycle (Figure 3A). Because the sum of all components in such a cycle must equal zero, the binding energy difference may be calculated as the difference in free energies:

$$\Delta\Delta G_{binding} = \Delta G_{binding}(B) - \Delta G_{binding}(A)$$
$$= \Delta G_{protein}(A \rightarrow B) - \Delta G_{water}(A \rightarrow B)$$

Models of structures **15b** and **15c** (Figure 3B) each in a monomeric complex with dCK and in solution alone were equilibrated using MC. The equilibrated structure of **15c** was subsequently perturbed into the structure of **15b** ("shrinking" the propyl chain into an ethyl) and vice versa ("growing" the ethyl chain into a propyl) using FEP. These calculations were performed using the MCPRO 2.0[41] software package. The free energy changes for these perturbations are illustrated in Figure 3C. Averaging the $\Delta\Delta G_{binding}$ obtained from the two

dx.doi.org/10.1021/jm400457y | J. Med. Chem. 2013, 56, 6696−6708

Table 3. In Vitro Biological Data in CEM Cells for Compounds 25−37[a]

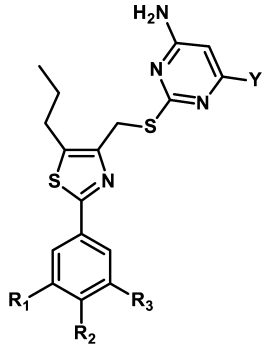

compd	R_1	R_2	R_3	Y	IC_{50} (nM) CEM cells
25	H	H	OCH_2CH_2OH	NH_2	2.45 (±0.778)
26	H	F	OCH_2CH_2OH	NH_2	1.07 (±0.230)
27	F	H	OCH_2CH_2OH	NH_2	2.83 (±1.628)
28	H	H	$OCH_2CH_2NHSO_2CH_3$	NH_2	11.58 (±3.353)
29	F	H	$OCH_2CH_2NHSO_2CH_3$	NH_2	8.01 (±0.230)
30	H	OCH_2CH_2OH	OCH_2CH_2OH	NH_2	2.59 (±1.146)
31	H	OCH_3	OH	NH_2	18.62[b]
32	H	OCH_3	$OCH_2CH_2CH_2OH$	NH_2	1.55 (±0.354)
33	H	OCH_3	OCH_2CH_2OH	NH_2	1.15 (±0.762)
34	H	OCH_3	OCH_2CH_2OH	H	2.90 (±0.300)
35	H	OCH_3	$OCH_2CH(CH_3)OH$	NH_2	2.85 (±0.071)
36	H	OCH_3	$OCH_2C(CH_3)_2OH$	NH_2	1.44 (±0.538)
37	H	OCH_3	$OCH_2CH_2NHSO_2CH_3$	NH_2	4.89 (±2.014)

[a]Inhibitory activity measured by ^{3}H-deoxycytidine (^{3}H-dC) uptake in CCRF-CEM human cells. Values reported are the mean ± SD of at least $n = 2$ independent experiments. [b]Value reported for $n = 1$.

simulations indicates that the propyl chain of **15c** confers a 1.210 kcal/mol more favorable free energy of binding in comparison to the ethyl chain of **15b**; this favorable effect is due to desolvation. The change in free energy upon extension of the alkyl chain is unfavorable both in the complex with the protein and in water alone (positive ΔG for chain lengthening, negative ΔG for chain shortening); however, the magnitude of the unfavorable ΔG is larger in solvent. The fact that this produces an overall favorable $\Delta\Delta G$ of binding suggests that the propyl chain is better able to exclude water from the interior cavity of the protein, allowing a greater association between the protein and the inhibitor.

Lead Optimization and SAR. Based on the potency trend in Table 2 and the existence of a hydrophobic pocket around the 5-position of the thiazole ring of **15a**, all further compounds in the SAR were made with the propyl chain installed at that position, to increase nonpolar interactions between the dCK enzyme pocket and the inhibitors. The fluorine atom terminating the ethoxy side-chain was substituted for a hydroxyl or sulfonamide group, with the goal of improving the molecule's solubility properties as well as potential hydrogen bonding interactions that might exist in the active site. Moreover, since inhibitory activity in L1210 and CCRF-CEM cells demonstrated the same trend in potency, the SAR for all subsequently synthesized compounds were examined only in CCRF-CEM cells. The results are summarized in Table 3.

Compounds **25**−**27** showed excellent (1−2 nM) potency against CCRF-CEM cells (Table 3). Substitution of the end-chain hydroxyl for a methyl sulfonamide resulted in a decrease in inhibitory activity of about 3-fold (compare **27** to **29**) or 5-fold (compare **25** to **28**). The initial SAR in Table 1 indicated that the presence of an alkoxy substituent at the para position led to increased inhibitory activity; therefore, the methoxy group was reinstalled at the para position. As expected, removal of the ethoxy side-chain (e.g., compound **31**) resulted in a substantially lower inhibitory activity, reinforcing the data observed for compounds **16**−**18** (Table 2). The presence of the methoxy moiety at the para position, in addition to the hydroxylethoxy side chain at the meta position, generated compound **33**, which has an inhibitory potency of 1 nM. To our surprise, removal of one of the amino groups from the pyrimidine ring led to a mere 2.5-fold decrease in inhibitory activity (compare **33** to **34**). Initially, we observed that removal of both amino groups from the pyrimidine ring resulted in complete loss of inhibitory activity (compounds **6** and **7**, Figure 1); however, the presence of one amino group can provide suitable key hydrogen bonding interactions to inhibit the enzyme. Compound **32**, which contains a side-chain that has been extended by one carbon to give a hydroxylpropoxy group, was also synthesized. However, this modification resulted in slightly decreased inhibitory activity in comparison with the hydroxylethoxy group. While compound **33** was a potent compound in cell culture, the presence of a primary hydroxyl group in the molecule raised concerns of a metabolic liability as a consequence of potential oxidation or glucuronidation.[42] Thus, compounds **35**−**37** were synthesized to decrease the possibility of metabolic degradation of **33**. Eight of these compounds in Table 3, whose IC_{50} values were lower than **15a** and whose structural properties suggested that they would have the best in vivo efficacy, were selected for further investigation.

Steady-State Kinetic Analysis of Selected dCK Inhibitors. In order to confirm that the cell-based values truly reflect the potency of the compounds we also determined the K_i^{app} values for select compounds using steady-state kinetic

dx.doi.org/10.1021/jm400457y | J. Med. Chem. 2013, 56, 6696−6708

assays. The cell-based assays indicated that compound **15a** was 6−12-fold (depending on the cell line used for the assay) less potent than compound **15c** (Table 2). Correspondingly, the steady-state data showed a 6-fold higher K_i^{app} value for compound **15a** (Table 4). Likewise, the low nanomolar IC_{50}

Table 4. Steady-State Kinetics of Selected dCK Inhibitors

compd	K_i^{app} (nM)	error (nM)	R^2
15a[a]	9.5	2.3	0.974
15c[a]	1.5	0.3	0.998
36	0.8	0.7	0.982
37	0.5	0.5	0.988

[a]Data from Nomme et al.

observed in CEM cells for compounds **36** and **37** (Table 3) was recapitulated in the steady-state kinetics derived K_i^{app} values for these compounds (Table 4). Hence, we conclude that our cell-based assays are providing us with relatively accurate data as to the strength of the interactions between the compounds and dCK.

Evaluation of in Vivo Inhibition of dCK Activity via a New PET PD Assay. The nucleoside analog PET probe ^{18}F-L-FAC is a high affinity substrate for dCK, which can be used to noninvasively estimate dCK enzymatic activity in vivo.[27] A schematic depicting the mechanism by which ^{18}F-L-FAC accumulates in cells in a dCK-specific manner is shown in Figure 4A. We reasoned that ^{18}F-L-FAC PET could be used to rapidly identify the most potent dCK inhibitors based on their effectiveness at inhibiting the accumulation of the ^{18}F-labeled dCK substrate PET tracer in various tissues. For the in vivo PET PD assay we selected dCK inhibitors that demonstrated 1−12 nM inhibitory activity in the cell culture ^{3}H-dC uptake assay (Table 3). Mice were treated with a single dose (50 mg/kg) of a given dCK inhibitor administered by intraperitoneal injection. Control mice received vehicle (40% Captisol in water) injections. Four hours later, treated mice were injected intravenously with ^{18}F-L-FAC; one hour after probe injection, mice were imaged by mPET/CT. The readout for the PET PD assay was the reduction in the accumulation of ^{18}F-L-FAC in dCK-positive tissues in dCK inhibitor versus vehicle treated mice. Previously, we showed that ^{18}F-L-FAC accumulates in a dCK-dependent manner into various tissues such as the thymus, spleen, bone marrow, and liver.[27] Accumulation in the bladder is a result of nonenzymatic renal clearance of the unmetabolized probe. Since the reproducibility in the dCK-dependent tissue retention of ^{18}F-L-FAC was most consistent in the liver,[27] we chose to quantify ^{18}F-L-FAC liver retention in order to compare the in vivo efficacy of the various dCK inhibitors. Optimal conditions for the PET PD assay were determined by performing a dose escalation and time course study using compound **33** (Supporting Figure S4).

Results from the ^{18}F-L-FAC mPET/CT scans are summarized in Figure 4. Transverse PET images of the ^{18}F-L-FAC liver scans for mice treated with either vehicle or compounds **15a**, **36**, or **37** are shown in Figure 4B. Figure 4C illustrates the uptake of ^{18}F-L-FAC in the livers of mice treated dCK inhibitors. The more efficacious compounds induced a greater reduction in the ^{18}F-L-FAC uptake relative to vehicle treatment, as a result of their greater inhibition of dCK-mediated phosphorylation of its ^{18}F-labeled substrate. Note the approximate 30% decrease in ^{18}F-L-FAC signal compared to vehicle control induced by compounds **28**, **29**, **36**, and **37**,

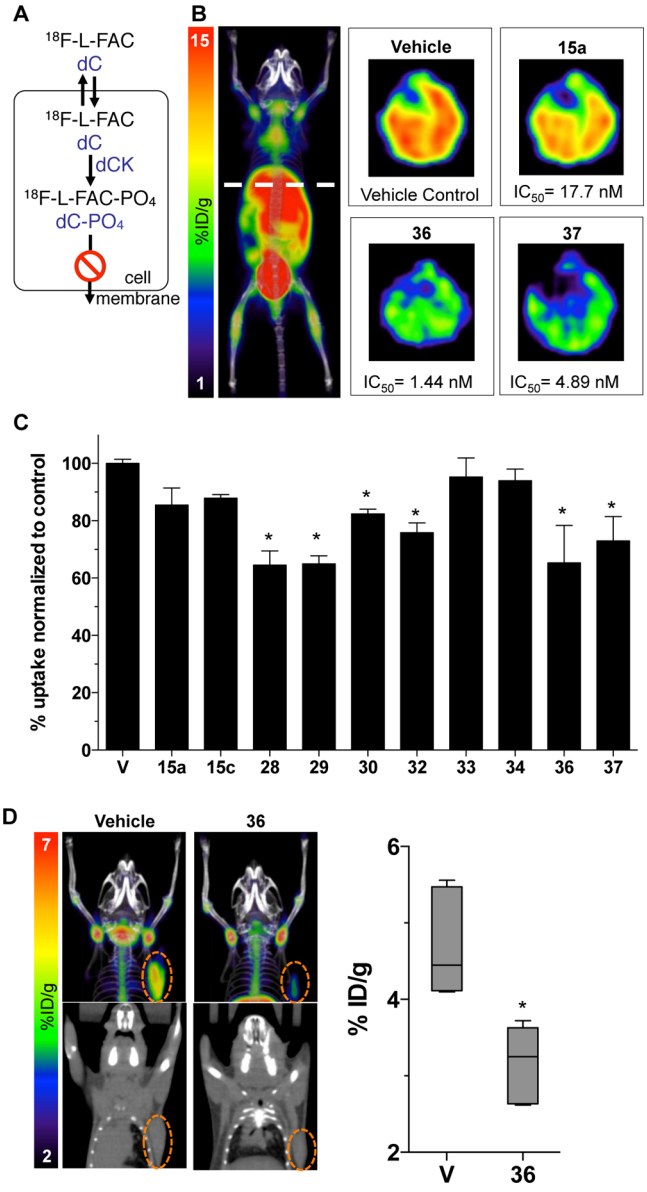

Figure 4. In vivo evaluation of dCK inhibitors via PET analysis. (A) Schematic of the mechanism by which ^{18}F-L-FAC accumulates in dCK expressing cells. (B) Representative transverse images of ^{18}F-L-FAC PET/CT liver scans of C57Bl/6 mice treated with compounds **15a**, **36**, and **37**. (C) Quantification of ^{18}F-L-FAC uptake in the liver for a sample of inhibitors with low nanomolar in vitro potency. Data are mean values ± SEM for at least n = 3 mice/group. *, $P < 0.03$. (D) Representative images and quantification of ^{18}F-L-FAC PET/CT scans of CCRF-CEM tumor bearing NSG mice that were treated with vehicle or compound **36**. Data are displayed as box and whisker plots for at least n = 4 mice/group. *, $P < 0.0012$.

indicating their superior in vivo efficacy relative to the other dCK inhibitor candidates. In addition, compounds **30** and **32** show about a 20% decrease in probe uptake. Compound **33**, one of the most potent dCK inhibitors in the cell culture assay (Table 3), showed poor in vivo efficacy in the ^{18}F-L-FAC liver PET assay, presumably due to its poor PK properties. As hypothesized, substitution of the hydroxyl group at the end of the ethoxy chain (e.g., compound **33**) for the metabolically stable methylsulfonamide (compounds **28**, **29**, and **37**) or hindering the hydroxyl group (compound **36**) proved advantageous for in vivo efficacy. Compounds **36** and **37** have the

dx.doi.org/10.1021/jm400457y | J. Med. Chem. 2013, 56, 6696−6708

lowest IC_{50} values among all the efficacious compounds and were chosen for further study. Here we focus on compound **36**, while compound **37** will be described in a subsequent publication (Nathanson, unpublished results).

Next we determined the efficacy of compound **36** at inhibiting dCK activity in tumor tissues in vivo. Mice bearing CCRF-CEM tumor xenografts were treated with compound **36** four hours prior to injection of ^{18}F-L-FAC (Figure 4D). One hour after the ^{18}F-L-FAC injection, mice were imaged by mPET/CT. The retention of ^{18}F-L-FAC in tumor xenografts from mice treated with compound **36** was reduced by about 30% compared to the retention of ^{18}F-L-FAC in tumors from vehicle treated mice (Figure 4D). To complement the PET assay, the pharmacokinetics of compound **36** was determined using standard analytical techniques, and the approximated values are reported in Figure 5.

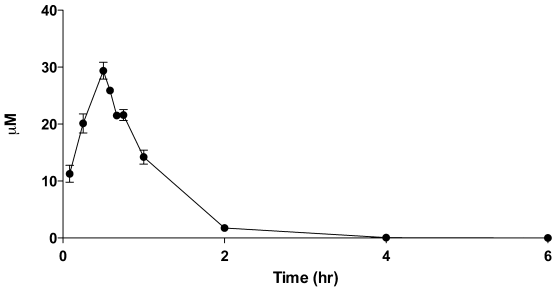

	Dose (mg/kg)	$AUC_{(0-t)}$ (mg/ml x min)	$T_{1/2}$ (min)	T_{max} (min)	C_{max} (μM)
36	50	.832	30	30	30

Figure 5. Pharmacokinetic profile of compound **36**. C57Bl/6 female mice were dosed with compound **36** via intraperitoneal injection. Dose formulation: 10% DMSO and 40% Captisol in water. Data are mean values ± SEM for n = 4 mice/time point.

X-ray Crystal Structure of Compound 36 Bound to Human dCK. X-ray crystallographic studies of compound **36** were initiated to obtain information about its binding to dCK. The crystal structure of the dCK:**36** complex was solved at 1.94 Å resolution (Figure 6 and Table 5). Similar to our observations for compound **15a** (Figure 2), in the case of **36**, the enzyme also adopts the open conformation. We observed one **36** molecule (green) in each protomer of the dimeric enzyme (Figure 6A). This is in contrast to the observation of two molecules bound per active site when the substituent at the 5-position is smaller than the propyl present in **36** (Figure 2, determinants of single versus double molecule binding to the dCK active site was analyzed by Nomme, unpublished results). Note that binding of **36** to dCK does not preclude nucleotide binding (UDP is shown in red, Figure 6A). The specific dCK:**36** interactions are shown in Figure 6B. These include an extensive hydrogen-bond network between the pyrimidine moiety of **36** and residues E53, Q97, and D133 in the dCK nucleoside binding site, as well as several hydrophobic interactions.

CONCLUSION

The identification of potent small molecule human dCK inhibitors that demonstrate in vivo target inhibition is reported. Optimization of inhibitory activity was achieved by extending an alkyl chain from the 5-position of the thiazole ring. In vivo efficacy was improved by manipulation of the ethoxy side-chain present at the meta position of the phenyl ring. The utility of PET as a powerful tool for noninvasive measure of target inhibition and, consequently, as a measure of *lack* of target inhibition (most likely due to substrate metabolism in vivo) is also presented. Although the major clinical applications of PET are primarily for central nervous system (CNS) and oncology-based diagnostics/therapeutics, PET is playing an increasingly important role in drug development, given the capability of this molecular imaging platform to address key challenges that include evaluation of biodistribution, absorption, target affinity, plasma binding, metabolism, and dosing.[43] Here we used the

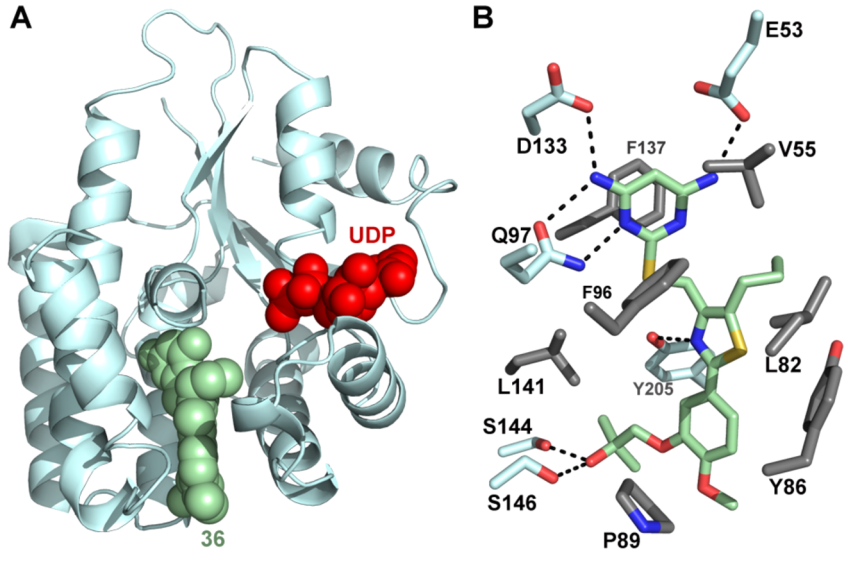

Figure 6. Crystal structure of the dCK:**36** complex. (A) Ribbon diagram of a dCK monomer (light blue) with the single observed molecule of **36** bound (green spheres) at the active site. The nucleotide UDP (red spheres) was also present in the complex. (B) Detail of the interactions between **36** and dCK. dCK residues involved in polar and hydrophobic interactions with **36** are colored in light blue and gray, respectively. Polar interactions are indicated as broken black lines.

dx.doi.org/10.1021/jm400457y | J. Med. Chem. 2013, 56, 6696−6708

Table 5. Data Collection and Refinement Statistics

parameter	comments
complex	**36** + UDP
PDB codes	4L5B
data collection statistics	
X-ray source and detector	LS-CAT ID-G MARCCD 300
wavelength (Å)	0.97856
temperature (K)	100
resolution[a] (Å)	1.94 (1.94−2.05)
number of reflections	
observed	206005
unique	40954
completeness (%)	99.2 (98.1)
R_{sym} (%)	4.5 (71.8)
average $I/\sigma(I)$	17.05 (2.05)
space group	P 4_1
unit cell (Å)	
$a = b$	68.67
c	120.02
refinement statistics	
refinement program	REFMAC5
twinning fraction	0.5
Rcryst (%)	18.8
Rfree (%)	23.3
resolution range (Å)	30−1.94
protein molecules per a.u.	2
number of atoms	
protein (ProtA, ProtB)	1932, 1925
inhibitor	32 × 2
UDP	25 × 2
water	75
r.m.s. deviation from ideal	
bond length (Å)	0.011
bond angles (deg)	1.647
average B-factors (Å2) /chain	
protein (ProtA, ProtB)	47.1, 47.3
inhibitor (ProtA, ProtB)	45.1, 43.4
UDP (ProtA, ProtB)	47.8, 44.7
waters	42.9
Ramachandran plot (%)	
most favored regions	89.1
additionally allowed regions	10.5
generously allowed regions	0.5
disallowed regions	0.0

[a]Last shell in parentheses.

radiotracer ^{18}F-L-FAC as a PET PD biomarker to compare the in vivo efficacies of candidate dCK inhibitors, first identified and characterized by potency in cell culture assays. Moreover, we used PET to provide estimates of in vivo target inhibition in CCRF-CEM xenograft mouse models by one of our most promising compounds, **36**. The ability of another promising compound, **37**, to elicit a significant pharmacological response against CCRF-CEM tumors with minimal toxicity to normal tissues was evaluated by our group and is described in a separate publication. Further optimization offering improvements to the PK and solubility properties of our best dCK inhibitors will be addressed in subsequent studies. In addition, the presence of fluorine on the aromatic ring of one of our most promising dCK inhibitors, **29**, makes it amenable to ^{18}F radiolabeling. Synthesizing a small molecule dCK inhibitor with an ^{18}F radioisotope could generate a positron-emitting version of the therapeutic candidate that can be detected and quantified noninvasively throughout the body of living individuals by PET imaging. This work will be the subject of a future communication.

EXPERIMENTAL SECTION

High-Throughput Screen. Recombinant human dCK at a concentration of 1 μM was incubated with 10 μM of drug, 10 μM of dC, and 0.5 μM ATP with 50 mM Tris (pH 7.6), 5 mM $MgCl_2$, and 2 mM DTT. The reaction was incubated at 37 °C for 4 h before adding CellTiter-Glo (Promega): Briefly, 40 μL of dCK enzyme were dispensed into 384 well plates (Greiner, Bahlingen, Germany) using a multidrop 384 (Thermo, Turku, Finnland) at concentration of 12.5 μg/mL; compounds were added using a Beckman-Coulter Biomek FX (Beckman Coulter, Brea, CA) equipped with a 500 nL custom pin tool (V&P Scientific, San Diego, CA). Columns 1, 2, 23, and 24 received only DMSO instead of any drugs. In addition, no dCK was added to column 23 and 24 as these columns served as additional controls (see below). After 30 min incubation at 37 °C, dC and ATP were added to a final concentration of 10 μM and 0.5 μM, respectively, for columns 1−22 using the multidrop in a volume of 10 μL. For columns 23 and 24 the following controls were used: 10 μL of a 2.5 μM ATP solution containing the following additional controls was added: for wells A-D23 1 μM dCTP, for wells E-H23 10 μM dCTP, for wells I-L23 10 μM L-FAC, for wells F-P23 10 μM FAC, for wells A-D24 0.5 μM ATP standard, for wells E-H24 0.1 μM ATP standard, for wells I-L24 1 μM DCK only, and for wells F-P24 10 μM UTP was added, respectively. These controls were included on each plate to exclude equipment failure. This was followed by a 4 h incubation at 37 °C and addition of 25 μL of Cell titer glo reagent (Promega, Fitchburg, WI) by multidrop followed by reading on an Acquest plate reader (Molecular Devices, Sunnyvale, CA). The libraries used were custom sets of compounds from the compound manufacturers Asinex (Winston-Salem, NC) and Enamine (Monmouth Jct., NJ). These sets consisted of compounds selected extensively for drug-likeness using the Lipinski rule of five, rotatable bonds, and maximal diversity using custom clustering algorithms.

Chemistry. General Procedures. Unless otherwise noted, reactions were carried out in oven-dried glassware under an atmosphere of nitrogen using commercially available anhydrous solvents. Solvents used for extractions and chromatography were not anhydrous. 4,6-Diamino-2-mercaptopyrimidine was obtained from drying the hydrate over dynamic vacuum at 110 °C for 20 h. All other reagents obtained from commercial suppliers were reagent grade and used without further purification unless specified. Reactions and chromatography fractions were analyzed by thin-layer chromatography (TLC) using Merck precoated silica gel 60 F_{254} glass plates (250 μm). Visualization was carried out with ultraviolet light, vanillin stain, permanganate stain, or *p*-anisaldehyde stain. Flash column chromatography was performed using E. Merck silica gel 60 (230−400 mesh) with compressed air. ^{1}H and ^{13}C NMR spectra were recorded on ARX500 (500 MHz) or Avance500 (500 MHz) spectrometers. Chemical shifts are reported in parts per million (ppm, δ) using the residual solvent peak as the reference. DMSO-d_6 (δ 2.50 ppm for ^{1}H; δ 39.5 ppm for ^{13}C) was used as the solvent and reference standards unless otherwise noted. The coupling constants, *J*, are reported in Hertz (Hz), and the resonance patterns are reported with notations as the following: br (broad), s (singlet), d (doublet), t (triplet), q (quartet), and m (multiplet). Electrospray mass spectrometry data were collected with a Waters LCT Premier XE time-of-flight instrument controlled by MassLynx 4.1 software. Samples were dissolved in methanol and infused using direct loop injection from a Waters Acquity UPLC into the Multi-Mode Ionization source. The purity of all final compounds was determined to be >95%. Analytical HPLC analysis was performed on a Knauer Smartline HPLC system with a Phenomenex reverse-phase Luna column (5 μm, 4.6 × 250 mm) with inline Knauer UV (254 nm) detector. Mobile phase: A: 0.1% TFA in H_2O, B: 0.1% TFA in MeCN. Eluent gradient is specified

dx.doi.org/10.1021/jm400457y | J. Med. Chem. 2013, 56, 6696−6708

for each described compound in the Supporting Information. All chromatograms were collected by a GinaStar (raytest USA, Inc.; Wilmington, NC, USA) analog to digital converter and GinaStar software (raytest USA, Inc.).

General Procedure for the Synthesis of Compounds 15a−c.

3-(2-Fluoroethoxy)-4-methoxybenzonitrile (20). To a solution of 3-hydroxy-4-methoxybenzonitrile **19** (3.0 g, 20.1 mmol) in DMF (100 mL) was added Cs_2CO_3 (10.5 g, 32.2 mmol) and 1-bromo-2-fluoroethane (5.1 g, 40.2 mmol). The mixture was stirred for 18 h at 50 °C. After concentration to remove residual solvent, the resulting residue was washed with brine and extracted with ethyl acetate. The organic layer was washed with water three times, dried over anhydrous $MgSO_4$ and concentrated in vacuo to yield crude **20** (3.91 g, 20.03 mmol, 99%) as a cream-colored solid. ^{1}H NMR (500 MHz, $CDCl_3$) δ: 7.28 (dd, J = 8.5, 2.0 Hz, 1H), 7.10 (d, J = 2.0 Hz, 1H), 6.90 (d, J = 8.5 Hz, 1H), 4.83−4.81 (m, 1H), 4.73−4.71 (m, 1H), 4.28−4.26 (m, 1H), 4.23−4.21 (m, 1H), 3.89 (s, 3H); ^{13}C NMR (125 MHz, $CDCl_3$) δ: 153.6, 148.1, 127.3, 119.1, 116.5, 111.9, 103.8, 82.3 (d, J_{CF} = 170.5 Hz), 68.7 (d, J_{CF} = 20.3 Hz), 56.1.

3-(2-Fluoroethoxy)-4-methoxybenzothioamide (21). To a mixture of **20** (3.86 g, 19.8 mmol) in pyridine (41 mL) and triethylamine (3 mL) was added ammonium sulfide solution (20% wt. in H_2O, 13.52 mL, 39.6 mmol). The mixture was stirred for 18 h at 60 °C. The reaction mixture was cooled and concentrated in vacuo to remove residual solvent. The resulting residue was washed with brine and extracted with ethyl acetate. The organic layer was dried over anhydrous $MgSO_4$ and concentrated in vacuo to yield **21** (4.5 g, 19.8 mmol, quantitative) as a yellow-orange solid. ^{1}H NMR (500 MHz, acetone-d_6) δ: 8.81 (brs, 1H), 8.74 (brs, 1H), 7.73 (s, 1H), 7.72 (dd, J = 8.5, 2.0 Hz, 1H), 7.00 (d, J = 8.0 Hz, 1H), 4.79 (dt, J = 48.0, 4.0 Hz, 2H), 4.32 (dt, J = 29.5, 4.0 Hz, 2H), 3.89 (s, 3H); ^{13}C NMR (125 MHz, acetone-d_6) δ: 200.4, 152.9, 147.2, 131.8, 121.5, 113.6, 110.8, 82.7 (d, J_{CF} = 167.3 Hz), 68.5 (d, J_{CF} = 19.6 Hz), 55.4.

Ethyl 2-(3-(2-Fluoroethoxy)-4-methoxyphenyl)-5-methylthiazole-4-carboxylate (22a). A mixture of thioamide **21** (1.50 g, 6.5 mmol) and ethyl 3-bromo-2-oxobutanoate (2.72 g, 13.0 mmol) in ethanol (32 mL) was stirred under refluxing conditions for 2.5 h. The resulting mixture was cooled and concentrated in vacuo to remove residual solvent. The crude residue was purified by flash column chromatography over silica gel (10:3 hexanes:ethyl acetate) to yield the desired thiazole intermediate **22a** (1.45 g, 4.3 mmol, 65%) as a light brown solid. ^{1}H NMR (500 MHz, DMSO-d_6) δ: 7.40 (dd, J = 8.5, 2.0 Hz, 1H), 7.37 (d, J = 2.0 Hz, 1H), 7.04 (d, J = 8.5 Hz, 1H), 4.72 (dt, J = 48.0, 4.0 Hz, 2H), 4.31−4.22 (m, 2H), 4.28 (q, J = 7.0 Hz, 2H), 3.81 (s, 3H), 2.67 (s, 3H), 1.28 (t, J = 7.0 Hz, 3H); ^{13}C NMR (125 MHz, DMSO-d_6) δ: 162.9, 162.1, 151.4, 148.2, 143.9, 141.9, 125.5, 120.5, 112.6, 110.8, 83.1 (d, J_{CF} = 165.9 Hz), 68.3 (d, J_{CF} = 19.0 Hz), 60.8, 56.0, 14.5, 13.3.

(2-(3-(2-Fluoroethoxy)-4-methoxyphenyl)-5-methylthiazol-4-yl)methanol (23a). To a stirred solution of intermediate **22a** (860 mg, 2.5 mmol) in CH_2Cl_2 (30 mL) cooled to 0 °C was added slowly diisobutylaluminum hydride (1.0 M in THF, 10 mmol, 10 mL). The reaction was allowed to warm to 23 °C and stirred for 1 h. The mixture was cooled to 0 °C and slowly quenched with a saturated aqueous solution of Rochelle's salt. The cloudy solution was stirred for 1 h at 23 °C until the solution became clear again. The resulting solution was extracted with ethyl acetate, washed with brine, dried over anhydrous magnesium sulfate, and concentrated in vacuo to give the desired alcohol **23a** (654 mg, 2.2 mmol, 88%) as a pale yellow solid. ^{1}H NMR (500 MHz, DMSO-d_6) δ: 7.39 (d, J = 2.0 Hz, 1H), 7.36 (dd, J = 8.5, 2.0 Hz, 1H), 7.02 (d, J = 8.5 Hz, 1H), 5.04 (t, J = 5.5 Hz, 1H), 4.73 (dt, J = 48.0, 3.5 Hz, 2H), 4.46 (d, J = 5.5 Hz, 2H), 4.25 (dt, J = 30.0, 3.5 Hz, 2H), 3.79 (s, 3H), 2.41 (s, 3H); ^{13}C NMR (125 MHz, DMSO-d_6) δ: 162.7, 153.2, 150.8, 148.2, 129.5, 126.5, 119.8, 112.5, 110.4, 83.1 (d, J_{CF} = 165.9 Hz), 68.4 (d, J_{CF} = 18.5 Hz), 57.3, 55.9, 11.2.

4-(Bromomethyl)-2-(3-(2-fluoroethoxy)-4-methoxyphenyl)-5-methylthiazole (24a). To a solution of **23a** (1.90 g, 6.4 mmol) in acetonitrile (30 mL) was added PPh_3 (2.5 g, 9.6 mmol) followed by hexabromoacetone (1.70 g, 3.2 mmol) at 23 °C. The mixture was stirred for 1 h at 40 °C when, by TLC analysis, all starting material had been consumed. The solvent was removed in vacuo, and the crude residue was purified by flash column chromatography over silica gel (10:3 hexanes:ethyl acetate) to give the desired bromide **24a** (1.84 g, 5.1 mmol, 80%) as a light brown solid. ^{1}H NMR (500 MHz, $CDCl_3$) δ: 7.50 (d, J = 2.0 Hz, 1H), 7.40 (dd, J = 8.5, 2.0 Hz, 1H), 6.88 (d, J = 8.0 Hz, 1H), 4.81 (dt, J = 47.0, 4.0 Hz, 2H), 4.59 (s, 2H), 4.36 (dt, J = 27.5, 4.0 Hz, 2H), 3.90 (s, 3H), 2.46 (s, 3H); ^{13}C NMR (125 MHz, $CDCl_3$) δ: 164.1, 151.2, 148.1, 148.0, 131.7, 126.4, 120.4, 111.6, 111.5, 82.4 (d, J_{CF} = 169.9 Hz), 68.4 (d, J_{CF} = 20.5 Hz), 55.9, 25.8, 11.4.

2-(((2-(3-(2-Fluoroethoxy)-4-methoxyphenyl)-5-methylthiazol-4-yl)methyl)thio)pyrimidine-4,6-diamine (15a). 4,6-Diamino-2-mercaptopyrimidine (336 mg, 2.36 mmol) and NaOH (94 mg, 2.36 mmol) were stirred in ethanol (20 mL) for 10 min at 23 °C. To the reaction mixture was added a solution of bromide **24a** (710 mg, 1.97 mmol) in hot ethanol (16 mL), and the resulting mixture was stirred for 3 h at 70 °C. The solution was cooled, concentrated in vacuo, and purified by flash column chromatography over silica gel (100:5 dichloromethane:methanol) to give the desired product **15a** (590 mg, 1.40 mmol, 71%) as a pale yellow solid. ^{1}H NMR (500 MHz, DMSO-d_6) δ: 7.36 (s, 1H), 7.34 (d, J = 8.0 Hz, 1H), 7.02 (d, J = 8.5 Hz, 1H), 6.09 (brs, 4H), 5.12 (s, 1H), 4.72 (dt, J = 48.0, 3.5 Hz, 2H), 4.32 (s, 2H), 4.25 (dt, J = 30.5, 3.5 Hz, 2H), 3.78 (s, 3H), 2.43 (s, 3H); ^{13}C NMR (125 MHz, DMSO-d_6) δ: 168.3, 163.9 (2), 163.3, 150.9, 149.5, 148.3, 129.1, 126.4, 119.9, 112.7, 110.5, 83.2 (d, J_{CF} = 165.9 Hz), 79.5, 68.5 (d, J_{CF} = 18.7 Hz), 56.1, 27.9, 11.7; HRMS-ESI (m/z) [M + H]$^+$ calcd for $C_{18}H_{20}FN_5O_2S_2$ H, 422.1121; found 422.1136.

2-(((5-Ethyl-2-(3-(2-fluoroethoxy)-4-methoxyphenyl)thiazol-4-yl)methyl)thio)pyrimidine-4,6-diamine (15b). ^{1}H NMR (500 MHz, DMSO-d_6) δ: 7.37 (dd, J = 8.0, 2.0 Hz, 1H), 7.36 (s, 1H), 7.02 (d, J = 8.5 Hz, 1H), 6.13 (brs, 4H), 5.13 (s, 1H), 4.72 (dt, J = 47.5, 4.0 Hz, 2H), 4.34 (s, 1H), 4.25 (dt, J = 30.5, 4.0 Hz, 2H), 3.79 (s, 3H), 2.87 (q, J = 7.5 Hz, 2H), 1.17 (t, J = 7.5 Hz, 3H); ^{13}C NMR (125 MHz, DMSO-d_6) δ: 168.2, 163.8 (2), 163.5, 151.0, 148.4, 148.3, 136.9, 126.5, 119.9, 112.7, 110.5, 83.3 (d, J_{CF} = 165.9 Hz), 79.5, 68.5 (d, J_{CF} = 18.8 Hz), 56.1, 28.0, 19.9, 17.1; HRMS-ESI (m/z) [M + H]$^+$ calcd for $C_{19}H_{22}FN_5O_2S_2$ H, 436.1277; found 436.1263.

2-(((2-(3-(2-Fluoroethoxy)-4-methoxyphenyl)-5-propylthiazol-4-yl)methyl)thio)pyrimidine-4,6-diamine (15c). ^{1}H NMR (500 MHz, acetone-d_6) δ: 7.53 (d, J = 2.0 Hz, 1H), 7.46 (dd, J = 8.5, 2.0 Hz, 1H), 7.03 (d, J = 8.5 Hz, 1H), 5.63 (brs, 4H), 5.38 (s, 1H), 4.80 (dt, J = 48.0, 4.0 Hz, 2H), 4.45 (s, 2H), 4.34 (dt, J = 29.5, 4.0 Hz, 2H), 3.87 (s, 3H), 2.91 (t, J = 7.5 Hz, 1H), 1.66 (qt, J = 7.5, 7.5 Hz, 2H), 0.97 (t, J = 7.5 Hz, 3H); ^{13}C NMR (125 MHz, acetone-d_6) δ: 169.2, 164.0 (2), 163.9, 163.6, 151.4, 149.0, 148.5, 134.6, 126.9, 119.8, 112.1, 111.1, 82.8 (d, J_{CF} = 167.5 Hz), 79.5, 68.6 (d, J_{CF} = 19.5 Hz), 55.3, 28.1, 25.2, 13.0; HRMS-ESI (m/z) [M + H]$^+$ calcd for $C_{20}H_{24}FN_5O_2S_2$ H, 450.1434; found 450.1432.

1-(5-(4-(((4,6-Diaminopyrimidin-2-yl)thio)methyl)-5-propylthiazol-2-yl)-2-methoxyphenoxy)-2-methylpropan-2-ol (36). ^{1}H NMR (500 MHz, MeOD) δ: 7.51 (d, J = 2.0 Hz, 1H), 7.39 (dd, J = 8.5, 2.0 Hz, 1H), 7.00 (d, J = 8.5 Hz, 1H), 5.48 (s, 1H), 5.32 (s, 1H), 4.48 (s, 2H), 3.89 (s, 3H), 3.86 (s, 2H), 2.88 (t, J = 7.5 Hz, 2H), 1.67 (qt, J = 7.5, 7.5 Hz, 2H), 1.33 (s, 6H), 0.98 (t, J = 7.5 Hz, 3H); ^{13}C NMR (125 MHz, MeOD) δ: 168.8, 165.2, 163.8 (2), 151.2, 148.9, 148.0, 135.4, 126.4, 119.7, 111.8, 110.7, 79.2, 77.0, 69.6, 55.2, 48.4, 27.9, 27.8, 25.0, 24.9, 12.6; HRMS-ESI (m/z) [M + H]$^+$ calcd for $C_{22}H_{29}N_5O_3S_2$ H, 476.1790; found 476.1772.

N-(2-(5-(4-(((4,6-Diaminopyrimidin-2-yl)thio)methyl)-5-propylthiazol-2-yl)-2-methoxyphenoxy)ethyl)-methanesulfonamide (37). ^{1}H NMR (500 MHz, DMSO-d_6) δ: 7.41 (dd, J = 7.5, 2.0 Hz, 1H), 7.39 (s, 1H), 7.25 (t, J = 6.0 Hz, 1H), 7.05 (d, J = 8.5 Hz, 1H), 6.13 (brs, 4H), 5.15 (s, 1H), 4.39 (s, 2H), 4.07 (t, J = 5.5 Hz, 2H), 3.80 (s, 3H), 3.36 (dt, J = 5.5, 5.5 Hz, 2H), 3.15 (d, J = 5.5 Hz, 1H), 2.98 (s, 3H), 2.84 (t, J = 7.5 Hz, 2H), 1.58 (qt, J = 7.5, 7.5 Hz, 2H), 0.91 (t, J = 7.5 Hz, 3H); ^{13}C NMR (125 MHz, DMSO-d_6) δ: 168.3, 163.9 (2), 163.7, 151.1,149.1, 148.3, 135.0, 126.5, 119.9, 112.7, 110.6, 79.5, 68.3, 60.2, 42.4, 31.2, 28.2, 28.0, 25.4,

dx.doi.org/10.1021/jm400457y | J. Med. Chem. 2013, 56, 6696−6708

13.9; HRMS-ESI (m/z) $[M + H]^+$ calcd for $C_{21}H_{28}N_6O_4S_3$ H, 525.1412; found 525.1404.

dCK Uptake Assay Performed in Cell Culture. The murine leukemic line L1210 was a gift from Charles Dumontet (Université Claude Bernard Lyon I, Lyon, France). The human lymphoma line CCRF-CEM was provided by Margaret Black (Washington State University). All L1210 and CCRF-CEM cell lines were cultured in RPMI medium 1640, supplemented with 5% FCS in a 5% CO_2 37 °C incubator. For the uptake assays cells were seeded at a density of 50,000 cells/well in Millipore MultiScreen GV 96 well plates. 0.25 μCi of ^{3}H-dC (Moravek Biochemicals) were added to the cells simultaneously with concentrations of dCK inhibitor at a final volume of 100 μL/well. After 1 h at 37 °C, cells were washed four times with ice cold phosphate-buffered saline (PBS) using the Millipore Vacuum Manifold. The amount of incorporated probe was measured by scintillation counting with the PerkinElmer Microbeta.

Protein Expression and Purification. Details on C4S S74E dCK variant expression and purification are detailed in Nomme et al.

Crystallization, X-ray Data Collection, and Refinement. Crystallization, data collection, and structure determination of dCK in complex with **15a** and **36** were performed following the general procedure as detailed in Nomme et al. Specifically for compound **36**, crystals of dCK in complex with UDP, $MgCl_2$ and a 2.5-fold excess of the **36** inhibitor were grown using the hanging drop vapor diffusion method at 12 °C. The reservoir solution contained 0.9−1.5 M trisodium citrate dehydrate and 25 mM HEPES (pH 7.5). Diffraction data were collected at the Advanced Photon Source, Argonne National Laboratory on Life Sciences-Collaborative Access Team (LS-CAT) beamlines 21 ID-G.

Kinetic Assay. Steady-state kinetic assay and data fitting were performed as described in Nomme et al.

Computational Modeling. All simulations were performed using the *MCPRO 2.0* package.[41] Initial coordinates were obtained from the X-ray structure of dCK in complex with compound **15c**. The protein was solvated in a 30 Å water cap, represented by the TIP4P[44] classical water model. Solute atoms represented by the OPLS-AA force field[45] were used. Equilibrations were performed using Metropolis Monte Carlo (MC) in the NPT ensemble at 25 °C and 1 atm. The backbone of the protein and all bond lengths within the protein were fixed; angles and torsions within 11 Å from the center of the bound molecule were sampled. All degrees of freedom of the inhibitor compound were sampled during equilibration simulations. Equilibration consisted of 5 × 10^6 configurations of sampling in which only solvent moves were allowed and of 10 × 10^6 subsequent configurations for the protein-inhibitor complex and for the lone inhibitor in solution. The equilibrated systems were then subject to free energy perturbation (FEP)/MC simulations. These simulations consisted of 14 perturbing steps of double-wide sampling. During FEP, the system underwent 5 × 10^6 configurations of solvent equilibration, followed by 10 × 10^6 configurations of full equilibration, and 25 × 10^6 configurations of data collection. All degrees of freedom of the inhibitor were sampled except those bonds undergoing perturbation. The perturbed bond lengths were systematically varied from the original to the final length.

In Vivo MicroPET/CT Imaging Studies. Animal studies were approved by the UCLA Animal Research Committee and were carried out according to the guidelines of the Department of Laboratory Animal Medicine at UCLA. For the PET liver assay, C57BL/6 mice were intraperitoneally (i.p.) injected with the indicated amounts of dCK inhibitor (resuspended in 40% Captisol) 4 h prior to intravenous injection of 70 μCi of ^{18}F-L-FAC. For the tumor xenograft assay, NOD scid IL-2 receptor gamma chain knockout (NSG) bearing subcutaneous CCRF-CEM tumor xenografts were injected with 50 mg/kg of compound **36** or vehicle. Four hours post-treatment mice were injected intravenously with 70 μCi of ^{18}F-L-FAC. For all mPET/CT studies, a 1 h interval was allowed between probe administration and mPET/CT scanning (Inveon, Siemens Medical Solutions USA Inc.; microCAT, Imtek Inc.). Static mPET images were acquired for 600 s. Images were analyzed using OsiriX Imaging Software Version 3.8.

Pharmacokinetic Studies. C57Bl/6 female mice, 8 weeks of age, were injected with a single dose of indicated compounds (50 mg/kg, i.p.). Blood samples (approximately 70 μL) were collected through retro-orbital bleeding into heparinized tubes at 5 min, 15 min, 30 min, 35 min, 40 min, 45 min, 1 h, 2 h, 4 h, and 6 h. The blood samples were centrifuged at 20,000g for 5 min to isolate plasma. One mL of acetonitrile was added to 30 μL of plasma. The supernatant was transferred to new tubes and was evaporated using a SpeedVac. Samples were then resuspended in 50 μL of neat DMSO, and supernatant was transferred to LC/MS sample vials. Samples were then run on an Agilent 6460 Triple Quad LC/MS.

Statistical Analyses. All statistics presented as means of biological replicates with standard error of the mean (±SEM), standard deviation (±SD), or box plots with max and min whiskers. P-value significances were calculated using one sample Student's t test function in GraphPad Prism 5 (GraphPad Software).

■ ASSOCIATED CONTENT

Ⓢ Supporting Information

Experimental details and spectroscopic data for compounds **8**−**14**, **16**−**18**, and **25**−**36**; synthetic schemes for **8a**, **8b**, and **37**; dose escalation/time course for PET assay. This material is available free of charge via the Internet at http://pubs.acs.org.

Accession Codes

Figures 2 and 3: dCK + **15a** + UDP Code: 4JLK; Figure 6: dCK + **36** + UDP Code: 4L5B

■ AUTHOR INFORMATION

Corresponding Author

*Phone: 310-825-1205. E-mail: CRadu@mednet.ucla.edu (C.G.R.). Phone: 312-355-5029. E-mail: Lavie@uic.edu (A.L.).

Present Addresses

○UCLA, Crump Institute for Molecular Imaging CNSI, 570 Westwood Plaza, Building 114, Box 951770, Mail Code: 177010, Los Angeles, CA 90095-1770.

▲Agensys, Inc. 1800 Stewart Ave, Santa Monica, CA, 90404.

◆Department of Radiology, Memorial Sloan-Kettering Cancer Center, New York, NY 10021, USA.

Author Contributions

‡These authors contributed equally.

Notes

The authors declare the following competing financial interest(s): C.G.R., J.C. and M.E.P. are co-founders of Sofie Biosciences, a molecular diagnostic company. They hold equity in Sofie Biosciences. The University of California also holds equity in Sofie Biosciences. Intellectual property that C.G.R. and J.C. invented and which was patented by the University of California has been licensed to Sofie Biosciences. The University of California has patented additional intellectual property invented by C.G.R., J.C., H.L., D.N., J.M.M., A.L.A., M.E.J., and A.L.

■ ACKNOWLEDGMENTS

We are extremely grateful to Dr. Nagichettiar Satyamurthy for his expert chemistry advice and support in designing the synthetic schemes, without his help this project would not have been possible. We thank Larry Pang and Michelle Tom for their assistance with PET/CT imaging studies, the UCLA Biomedical Cyclotron crew for producing ^{18}F-L-FAC, and Radha Bathala for her assistance in synthesizing compound intermediates. We would also like to acknowledge Jong Lee at the UCLA Molecular Screening Shared Resource for assistance with the high-throughput screening. J.M.M. and D.N. thank the Scholars in Oncologic Molecular Imaging program for postdoctoral fellowships. This work was funded by In Vivo

Cellular and Molecular Imaging Centers Developmental Project Award National Institutes of Health P50 CA86306 (C. G. Radu, H. R. Herschman, and W. R. Austin) and the US National Cancer Institute grant 5U54 CA119347 (C. G. Radu). R.D. would like to acknowledge support for the Molecular Screening Shared Resource from the National Cancer Center Support grant P3016042-35 (J. Gasson).

■ ABREVIATIONS USED

ADA, adenosine deaminase; dCK, deoxycytidine kinase; dNTP, deoxyribonucleotide triphosphate; ^{18}F-FAC, ^{18}F-1-(2′-deoxy-2′-FluoroArabinofuranosyl) Cytosine; TK1, thymidine kinase 1; HTS, high throughput screen; dC, deoxycytidine; dG, deoxyguanosine; dA, deoxyadenosine; ^{18}F-FDG, 2-^{18}F-fluoro-2-deoxy-D-glucose; ^{18}F-L-FAC, ^{18}F-L-1-(2′-deoxy-2′-FluoroArabinofuranosyl) Cytosine; ^{3}H-dC, ^{3}H-deoxycytidine; ATP, adenosine triphosphate; UTP, uridine triphosphate; UDP, uridine diphosphate; E53, glutamic acid 53; D133, aspartic acid 133; Q97, glutamine 97; V55, valine 55; L82, leucine 82; F96, phenylalanine 96; mPET/CT, micro positron emission tomography/computed tomography; PK, pharmacokinetic; PD, pharmacodynamic; DMF, dimethylformamide; DIBAL-H, diisobutylaluminum hydride; EtOH, ethanol; Rochelle's Salt, sodium potassium tartrate; DMSO, dimethylsulfoxide; PBS, phosphate-buffered saline; FCS, fetal calf serum

■ REFERENCES

(1) Reichard, P. Interactions between Deoxyribonucleotide and DNA Synthesis. *Annu. Rev. Biochem.* **1988**, *57*, 349−374.
(2) Arner, E. S. J.; Eriksson, S. Mammalian Deoxyribonucleoside Kinases. *Pharmacol. Ther.* **1995**, *67*, 155−186.
(3) Sabini, E.; Hazra, S.; Ort, S.; Konrad, M.; Lavie, A. Structural Basis for Substrate Promiscuity of dCK. *J. Mol. Biol.* **2008**, *378*, 607−621.
(4) Pasti, C.; Gallois-Montbrun, S.; Munier-Lehmann, H.; Vernon, M.; Gilles, A. M.; Deville-Bonne, D. Reaction of Human UMP-CMP Kinase with Natural and Analog Substrates. *Eur. J. Biochem.* **2003**, *270*, 1784−1790.
(5) Krishnan, P.; Gullen, E. A.; Lam, W.; Dutschman, G. E.; Grill, S. P.; Cheng, Y. C. Novel Role of 3-Phosphoglycerate Kinase, a Glycolytic Enzyme, in the Activation of L-Nucleoside Analogs, a New Class of Anticancer and Antiviral Agents. *J. Biol. Chem.* **2003**, *278*, 36726−36732.
(6) Toy, G.; Austin, W. R.; Liao, H.-I.; Cheng, D.; Singh, A.; Campbell, D. O.; Ishikawa, T.-o.; Lehmann, L. W.; Satyamurthy, N.; Phelps, M. E.; Herschman, H. R.; Czernin, J.; Witte, O. N.; Radu, C. G. Requirement for Deoxycytidine Kinase in T and B Lymphocyte Development. *Proc. Natl. Acad. Sci. U.S.A.* **2010**, *107*, 5551−5556.
(7) Austin, W. R.; Armijo, A. L.; Campbell, D. O.; Singh, A. S.; Hsieh, T.; Nathanson, D.; Herschman, H. R.; Phelps, M. E.; Witte, O. N.; Czernin, J.; Radu, C. G. Nucleoside Salvage Pathway Kinases Regulate Hematopoiesis by Linking Nucleotide Metabolism with Replication Stress. *J. Exp. Med.* **2012**, *209*, 2215−2228.
(8) Van Rompay, A. R.; Johansson, M.; Karlsson, A. Substrate Specificity and Phosphorylation of Antiviral and Anticancer Nucleoside Analogs by Human Deoxyribonucleoside Kinases and Ribonucleoside Kinases. *Pharmacol. Ther.* **2003**, *100*, 119−139.
(9) Yang, C.; Lee, M.; Hao, J.; Cui, X.; Guo, X.; Smal, C.; Bontemps, F.; Ma, S.; Liu, X.; Engler, D.; Parker, W. B.; Xu, B. Deoxycytidine Kinase Regulates the G2/M Checkpoint through Interaction with Cyclin-Dependent Kinase 1 in Response to DNA Damage. *Nucleic Acids Res.* **2012**, *40* (19), 9621−32.
(10) Tarver, J. E.; Jessop, T. C.; Carlsen, M.; Augeri, D. J.; Fu, Q.; Healy, J. P.; Heim-Riether, A.; Xu, A.; Taylor, J. A.; Shen, M.; Keyes, P. E.; Kimball, S. D.; Yu, X.-C.; Miranda, M.; Liu, Q.; Swaffield, J. C.; Nouraldeen, A.; Wilson, A. G. E.; Rinch, R.; Jhaver, K.; Foushee, A. M. D.; Anderson, S.; Oravecz, T.; Carson, K. G. 5-Fluorocytosine Derivatives as Inhibitors of Deoxycytidine Kinase. *Bioorg. Med. Chem. Lett.* **2009**, *19*, 6780−6783.
(11) Yu, X.-C.; Miranda, M.; Liu, Z.; Patel, S.; Nguyen, N.; Carson, K.; Liu, Q.; Swaffield, J. C. Novel Potent Inhibitors of Deoxycytidine Kinase Identified and Compared by Multiple Assays. *J. Biomol. Screening* **2010**, *15*, 72−79.
(12) Ward, A. D.; Baker, B. R. Irreversible Enzyme Inhibitors: Active-Site-Directed Inhibitors of Deoxycytidine Kinase. *J. Med. Chem.* **1977**, *20*, 88−92.
(13) Jessop, T. C.; Tarver, J. E.; Carlsen, M.; Xu, A.; Healy, J. P.; Heim-Riether, A.; Fu, Q.; Taylor, J. A.; Augeri, D. J.; Shen, M.; Stouch, T. R.; Swanson, R. V.; Tari, L. W.; Hunger, M.; Hoffman, I.; Keyes, P. E.; Yu, X.-C.; Miranda, M.; Liu, Q.; Swaffield, J. C.; Kimball, S. D.; Nouraldeen, A.; Wilson, A. G. E.; Foushee, A. M. D.; Jhaver, K.; Finch, R.; Anderson, S.; Oravecz, T.; Carson, K. G. Lead Optimization and Structure-based Design of Potent and Bioavailable Deoxycytidine Kinase Inhibitors. *Bioorg. Med. Chem. Lett.* **2009**, *19*, 6784−6787.
(14) Weber, W. A.; Grosu, A. L.; Czernin, J. Technology Insight: Advances in Molecular Imaging and an Appraisal of PET/CT Scanning. *Nat. Clin. Pract. Oncol.* **2008**, *5*, 160−170.
(15) Czernin, J.; Benz, M. R.; Allen-Auerbach, M. S. PET/CT Imaging: The Incremental Value of Assessing the Glucose Metabolic Phenotype and the Structure of Cancers in a Single Examination. *Eur. J. Radiol.* **2010**, *73*, 470−480.
(16) Gambhir, S. S. Molecular Imaging of Cancer with Positron Emission Tomography. *Nat. Rev. Cancer* **2002**, *2*, 683−693.
(17) Rigo, P.; Paulus, P.; Kaschten, B. J.; Hustinx, R.; Bury, T.; Jerusalem, G.; Benoit, T.; Foidart Willems, J. Oncological Application of Positron Emission Tomography with Fluorine-18. *Eur. J. Nucl. Med.* **1996**, *23*, 1641−1674.
(18) Wood, K. A.; Hoskin, P. J.; Saunders, M. I. Positron Emission Tomography in Oncology: A Review. *Clin. Oncol.* **2007**, *19*, 237−255.
(19) Weber, W. A. Positron Emission Tomography as an Imaging Biomarker. *J. Clin. Oncol.* **2006**, *24*, 3282−3292.
(20) Oriuchi, N.; Higuchi, T.; Ishikita, T.; Miyakubo, M.; Hanaoka, H.; Iida, Y.; Endo, K. Present Role and Future Prospects of Positron Emission Tomography in Clinical Oncology. *Cancer Sci.* **2006**, *97*, 1291−1297.
(21) Jadvar, H.; Alavi, A.; Gambhir, S. S. ^{18}F-FDG Uptake in Lung, Breast, and Colon Cancers: Molecular Biology Correlates and Disease Characterization. *J. Nucl. Med.* **2009**, *50*, 1820−1827.
(22) Hargreaves, R. J. The Role of Molecular Imaging in Drug Discovery and Development. *Clin. Pharmacol. Ther.* **2008**, *83*, 349−353.
(23) Wang, J. L.; Maurer, L. Positron Emission Tomography: Applications in Drug Discovery and Drug Development. *Curr. Top. Med. Chem.* **2005**, *5*, 1053−1075.
(24) Wagner, C. C.; Muller, M.; Lappin, G.; Langer, O. Positron Emission Tomography for Use in Microdosing Studies. *Curr. Opin. Drug Discovery Dev.* **2008**, *11*, 104−110.
(25) Laing, R. E.; Walter, M. A.; Campbell, D. O.; Herschman, H. R.; Satyamurthy, N.; Phelps, M. E.; Czernin, J.; Witte, O. N.; Radu, C. R. Noninvasive Prediction of Tumor Responses to Gemcitabine using Positron Emission Tomography. *Proc. Natl. Acad. Sci. U.S.A.* **2009**, *106*, 2847−2852.
(26) Radu, C. G.; Shu, C. J.; Nair-Gill, E.; Shelly, S. M.; Barrio, J. R.; Satyamurthy, N.; Phelps, M. E.; Witte, O. N. Molecular Imaging of Lymphoid Organs and Immune Activation by Positron Emission Tomography with a New [^{18}F]-Labeled 2'-Deoxycytidine Analog. *Nat. Med.* **2008**, *14*, 783−788.
(27) Shu, C. J.; Campbell, D. O.; Lee, J. T.; Tran, A. Q.; Wengrod, J. C.; Witte, O. N.; Phelps, M. E.; Satyamurthy, N.; Czernin, J.; Radu, C. R.; Novel, P. E. T. Probes Specific for Deoxycytidine Kinase. *J. Nucl. Med.* **2010**, *51*, 1092−1098.
(28) Fan, F.; Wood, K. V. Bioluminescent Assays for High-Throughput Screening. *Assay Drug Dev. Technol.* **2007**, *5*, 127−136.
(29) Müller, K.; Faeh, C.; Diederich, F. Fluorine in Pharmaceuticals: Looking Beyond Intuition. *Science* **2007**, *317*, 1881−1886.

(30) Park, B. K.; Kitteringham, N. R.; O'Neill, P. M. Metabolism of Fluorine-Containing Drugs. *Annu. Rev. Pharmacol. Toxicol.* **2001**, *41*, 443−470.
(31) Crane, L. J.; Anastassiadou, M.; Stigliani, J.-L.; Baziard-Mouysset, G.; Payard, M. Reactions of Some Ortho and Para Halogenated Aromatic Nitriles with Ethylenediamine: Selective Synthesis of Imidazolines. *Tetrahedron* **2004**, *60*, 5325−5330.
(32) Okonya, J. F.; Hoffman, R. V.; Johnson, M. C. Synthesis of 2-Oxazolone-4-Carboxylates from 3-Nosyloxy- and 3-Bromo-2-ketoesters. *J. Org. Chem.* **2002**, *67*, 1102−1108.
(33) Trullinger, T. K.; Hunter, R.; Garizi, N.; Yap, M. C. H.; Buysse, A. M.; Pernich, D.; Johnson, T. C.; Bryan, K.; Deamicis, C.; Zhang, Y.; Niyaz, N. M.; McLeod, C. L.; Ross, R.; Zhu, Y.; Johnson, P. L.; Eckelbarger, J. D.; Parker, M. H. Pesticidal Compositions. Patent application US 2010/0292253 A1.
(34) Joseph, K. M.; Larraza-Sanchez, I. Synthesis of Benzyl Bromides with Hexabromoacetone: An Alternative Path to Drug Intermediates. *Tetrahedron Lett.* **2011**, *52*, 13−16.
(35) Laxer, A.; Major, D. T.; Gottlieb, H. E.; Fischer, B. ($^{15}N_5$)-Labeled Adenine Derivatives: Synthesis and Studies of Tautomerism by ^{15}N NMR Spectroscopy and Theoretical Calculations. *J. Org. Chem.* **2001**, *66*, 5463−5481.
(36) Chottiner, E. G.; Shewach, D. S.; Datta, N. S.; Ashcraft, E.; Gribbin, D.; Ginsburg, D.; Fox, I. H.; Mitchell, B. S. Cloning and Expression of Human Deoxycytidine Kinase cDNA. *Proc. Natl. Acad. Sci. U.S.A.* **1991**, *88*, 1531−1535.
(37) Shewach, D. S.; Reynolds, K. K.; Hertel, L. Nucleotide Specificity of Human Deoxycytidine Kinase. *Mol. Pharmacol.* **1992**, *42*, 518−524.
(38) Metropolis, N.; Ulam, S. The Monte Carlo Method. *J. Am. Stat. Assoc.* **1949**, *44*, 335−341.
(39) Zwanzig, R. W. High-Temperature Equation of State by a Perturbation Method. *J. Chem. Phys.* **1954**, *22*, 1420−1426.
(40) Jorgensen, W. L.; Thomas, L. L. Perspective on Free-Energy Perturbation Calculations for Chemical Equilibria. *J. Chem. Theory Comput.* **2008**, *4*, 869−876.
(41) Jorgensen, W. L.; Tirado-Rives, J. Molecular Modeling of Organic and Biomolecular Systems Using BOSS and MCPRO. *J. Comput. Chem.* **2005**, *26*, 1689−1700.
(42) Shu, Y. Z.; Johnson, B. M.; Yang, T. J. Role of Biotransformation Studies in Minimizing Metabolism-Related Liabilities in Drug Discovery. *AAPS J.* **2008**, *10*, 178−192.
(43) Bhattacharyya, S. Application of Positron Emission Tomography in Drug Development. *Biochem. Pharmacol.* **2012**, *1*, 1000e128.
(44) Jorgensen, W. L.; Chandrasekhar, J.; Madura, J. D.; Impey, R. W.; Klein, M. L. Comparison of Simple Potential Functions for Simulating Liquid Water. *J. Chem. Phys.* **1983**, *79*, 926−935.
(45) Jorgensen, W. L.; Maxwell, D. S.; Tirado-Rives, J. Development and Testing of the OPLS All-Atom Force Field on Conformational Energetics and Properties of Organic Liquids. *J. Am. Chem. Soc.* **1996**, *118*, 11225−11236.